Journal of Physics D:
Applied Physics

PAPER • **OPEN ACCESS**

Neutral gas temperature of adamantane in a radio-frequency inductively coupled plasma electrothermal micro-thruster using optical emission spectroscopy

To cite this article: Thimthana Lee *et al* 2025 *J. Phys. D: Appl. Phys.* **58** 115206

OPEN ACCESS
IOP Publishing
Journal of Physics D: Applied Physics
J. Phys. D: Appl. Phys. **58** (2025) 115206 (16pp)
https://doi.org/10.1088/1361-6463/ada6c9

Neutral gas temperature of adamantane in a radio-frequency inductively coupled plasma electrothermal micro-thruster using optical emission spectroscopy

Thimthana Lee*, Mahdi Davoodianidalik, Dimitrios Tsifakis, Roderick W Boswell and Christine Charles

Space Plasma Power and Propulsion Laboratory, The Australian National University, Canberra 2601, ACT, Australia

E-mail: thimthana.lee@anu.edu.au

Received 11 November 2024, revised 17 December 2024
Accepted for publication 7 January 2025
Published 17 January 2025

Abstract

The gas temperature of adamantane plasma in a 13.56 MHz radio-frequency (RF) inductively coupled plasma was measured using optical emission spectroscopy. Rovibrational band fitting of the Second Positive System of nitrogen gas (N_2) from the addition of N_2 and Swan system of homo-nuclear carbons (C_2) from adamantane dissociation were used to obtain the gas temperature through the rotational temperature under the assumption of rotational-translational equilibrium. The measured temperature ranged from 400 to 700 K, increasing with RF power range from 10 to 100 W and adamantane flow rate from 0.25 to 1 mg s^{-1}, with discharge pressures up to a few Torr. The energy released during adamantane dissociation contributed to a slight temperature increase compared to conventional pure N_2 plasma. Adding a large amount of helium (He) acted as a quencher, reducing the gas temperature. In an adamantane-He mixture, the gas temperature remained stable at mid-range power and at lower adamantane flow rates. Justification of gas temperature and a simple power balance model were described. Applications of adamantane spectroscopy include propulsion, plasma processing, and astrophysics, with the inclusion of future studies.

Supplementary material for this article is available online

Keywords: adamantane, optical emission spectroscopy, gas temperature determination, electrothermal plasma thruster, C_2 Swan bands

* Author to whom any correspondence should be addressed.

1. Introduction

Electric propulsion systems have emerged as promising space thrusters, offering better specific impulse compared to classical cold-gas thrusters or chemical rockets [1]. Recently, an electrothermal plasma micro-thruster, known as the Pocket Rocket (PR), was developed with the aim of heating neutral gas through ion-neutral charge exchange (I-N CEX) collisions. This occurs within a cylindrical plasma cavity operating at pressures of a few Torr and excited by a 13.56 MHz radio-frequency (RF) field [2, 3]. With RF power under 100 W, the thrust or specific impulse has shown a 200% increase [2], attributed to the rise in gas temperature as confirmed through both analytical modelling [3] and indirect measurement techniques [4]. However, directly measuring gas temperature with thermal probes presents challenges due to interference from the plasma's electromagnetic field, often leading to inaccurate readings.

Optical emission spectroscopy (OES) is one of the indirect measurement techniques to determine the gas temperature from the emission of non-equilibrium plasmas. Under the assumption of rotational-translational thermalisation, the rotational temperature derived from rovibronic (rotation + vibration + electronic) transitions distribution in molecular spectra can be equivalent to the translational, or gas, temperature [5]. Another approach such as thermal Doppler broadening assesses gas temperature by evaluating the broadening of atomic spectral lines, though it requires a high-resolution spectrometer to resolve these line widths accurately [4]. For rovibrational molecular spectra, laser-induced fluorescence (LIF) is a frequently used active diagnostic tool due to its accuracy in temperature measurement, although its complexity poses experimental challenges [5, 6]. In plasma environments, the laser is not needed as excited state molecules normally occur by collisions between molecules and electrons, thereby promoting the feasibility of using passive diagnostic techniques.

Among the rovibrational spectra, the Second Positive System (SPS) of N_2 ($C^3\Pi_g \rightarrow B^3\Pi_u$) is the most commonly used for diagnostics in diatomic molecules due to the extensive literature available on it [5, 7–10]. When N_2 is absent from the plasma, a small addition of N_2 is typically sufficient to produce the N_2 spectra without altering the plasma conditions [6, 11, 12]. Another diatomic species of interest is the C_2 Swan band system ($d^3\Pi_g \rightarrow a^3\Pi_u$)[1], where it is commonly used in the carbon-rich plasmas [14–18]. In many case studies, argon (Ar) is widely favoured for OES-based gas temperature determination [19–21]. For instance, Greig *et al* effectively applied this technique to estimate Ar temperature in a PR thruster [4]. Recently, seeking a PR alternative propellant particularly targeting the solid hydrocarbons has garnered interest as they offer storage and cost-effective advantages [22]. Dietz *et al* reported the promising performance of a hydrocarbon called adamantane in an ion-gridded thruster [23], highlighting its potential as an alternative propellant for a PR thruster.

Adamantane ($C_{10}H_{16}$) is the smallest diamondoid, characterised by its aliphatic, fused cyclopentane rings and saturated carbon bonds. This molecule appears as a white crystalline solid that sublimates at room temperature [22]. Adamantane can be found naturally as a by-product of petroleum processing or synthesised in the laboratory. The structure of adamantane is tetrahedral symmetric (T_d), providing it with at least 219 degrees of freedom (3 translational modes, 3 rotational modes inherent to T_d symmetry, 72 fundamental vibrational modes calculated as $3N-6$, where N is the number of atoms) [24]. This high degree of freedom introduces considerable complexity in analysing its spectroscopic properties. Adamantane has an ionisation threshold of 9.23 eV recorded in the NIST database and was later supported by [25].

Direct thrust measurements of adamantane as a cold-gas thruster have recently been explored together with other similar propellants [22]. Although adamantane has a great value in terms of storage density leading to a higher effective specific impulse compared to gaseous propellants, its low specific impulse of ∼20 s at a few milligrams per second remains a notable challenge. To improve thruster performance, electrothermal plasma propulsion is proposed as a means to increase the temperature of adamantane. To date, very few studies have investigated the optical emission spectra of adamantane. Dietz *et al* reported an adamantane spectrum with a fair resolution, noting some impurities in the thruster discharge [23]. Previously, Stauss *et al* observed C_2 and CH bands in diamondoid synthesis within a plasma microreactor, indicating multiple fragmentation pathways of adamantane [26]. Candian *et al* further confirmed the dissociation processes and calculated the appearance energies of those fragment ions [25]. Mass spectrometry studies revealed multiple fragmentation channels from C_3H_x to C_7H_x abundantly observed at higher electron energies [23, 25, 27]. Other studies have concentrated on the mid-to-near infrared (IR) spectrum [24, 27], and the vacuum ultraviolet (VUV) range [25] to accurately characterise adamantane fragment structures, as energy absorption typically occurs within these rotational and vibrational modes in these spectral ranges.

In this paper, OES was employed to determine the rotational temperature of adamantane spectra in the visible (VIS) range (300–900 nm) using an RF inductively coupled plasma (ICP) thruster operating at pressures from 100 to 1 Torr. Initial rovibrational fittings of the SPS bands were conducted with pure N_2 plasma to validate the measurement. Subsequently, trace amounts of N_2 were added to determine the gas temperature including the effect of adamantane flow. C_2 Swan bands were also investigated by adding helium (He) as a buffer gas. The rationale for adding a buffer gas in this work, which will be further detailed in section 4.3, is to enhance the C_2 emission intensity, as carbon-based spectra are relatively weak. The implications of determining adamantane temperature were discussed across various applications. The fitting process throughout this study utilised the open-source software MassiveOES [28–30], with a supplemental database for Swan

[1] Old texts refer to this transition as $A^3\Pi_g \rightarrow X^3\Pi_u$ [13]. This mislabeling of the Swan band transition was originated from the confusion with different naming conventions for electronic states, particularly in early spectroscopy literature.

bands contributed by Carbone *et al* [16]. Atomic lines for H, He, N, and C were referenced from the NIST database [31], while molecular band heads for SPS and Swan systems were identified using the standard handbook [13].

2. Experimental setup

A schematic diagram of the experimental setup, as illustrated in figure 1, is conducted in a LAMWICH vacuum chamber which was described in detail elsewhere [22]. Briefly, a 30 l stainless steel vessel is connected to a $40\,m^3\,hr^{-1}$ roughing pump and a $3801\,s^{-1}$ turbo-molecular pump, which together can evacuate the chamber down to $\sim10^{-5}$ Torr. Chamber pressure is measured by a nitrogen-calibrated Convectron® vacuum gauge and an ion gauge. During operation, the ion gauge was deactivated to prevent filament damage from adamantane vapour. The cold trap was installed between the two pumps to capture a condensible vapour from contaminating the working oil inside the rough pump.

A ∼6 mm inner diameter, ∼2 mm thick, and ∼50 mm long alumina discharge tube is wrapped by a 25-turn, 1 mm diameter, ∼30 mm long antenna made of copper wire, yielding an inductance of ∼2300 nH (measured by antenna analyser). One end of the coil is grounded at the expansion chamber side (RHS on figure 1), while the other end is powered by the RF source located half-way along the discharge tube. This end is connected to a $\sim25\,cm^3$ cylindrical plenum where rare gases and adamantane vapour are injected (LHS on figure 1). A matching box consisting of two variable capacitors matches the inductive load including the plasma with a 50 Ω source impedance. The matched circuit is then connected to a 13.56 MHz ACG-5 RF generator, providing a maximum output of 500 W. It is monitored by a CN-801 standing wave ratio (SWR) meter, where the forwarded power and reflected power are read. The matching network was tuned for all experiments to minimise the reflected power once plasma was ignited. For most cases, retuning was made at ∼60 W of RF power as the SWR shifts to ∼3.

N_2 and He gases are introduced into the plenum via a quarter-inch nylon tube. For N_2, the gas flow is controlled and monitored by an MKS Mass-Flo® controller (MFC) and MKS Type 247 C multi-channel readout, providing accurate flow rates up to 20 SCCM with a precision of 0.01 SCCM. Since N_2 is factory calibrated, no gas correction is needed. Helium is regulated by an Alicat MC series gas flow meter up to 500 SCCM after calibration. Adamantane vapour flow, on the other hand, is controlled by adjusting the temperature of a propellant tank (labelled as HC in the figure where HC stands for hydrocarbon), as previously detailed in [22]. Solid adamantane purchased from Sigma-Aldrich© is stored in a tank of $\sim60.8\,cm^3$ volume, equipped with an electrical heater and thermocouple for precise temperature control. The electrical heaters and thermocouples are installed from the tank to the discharge in order to accurately control the temperature of the system. Unlike prior setups, the tank is exposed to ambient air, contributing to heat loss; therefore, an insulator has been added to mitigate the effect of convection.

To measure optical spectra, the light emission is collected by an OES system composed of a viewport, an optical fibre, and a spectrometer. The plenum has a viewport aligned concentrically with the discharge tube and is made of MgF_2, which enables excellent transmission across the VIS spectrum (200–900 nm). An initial survey of the emission spectra of adamantane, He, and N_2 was performed using a low-resolution Ocean Optics QE65000 spectrometer with a resolution of ∼2 nm, as shown in figure 2. The spectrum of pure adamantane (blue) confirms the existence of weak C_2 Swan bands between 460 and 560 nm (with intensity 100 times weaker than that of N_2 and He) and several other fragmented spectra. Notably, a Swan system has the strongest band head at 516 nm where a vibrational transition of $\Delta v = 0$ is accommodated (more detail will be discussed later). The most substantial peak at 656 nm is identified as H-Balmer alpha (H_α), indicating hydrogen losses from adamantane dissociations. CH bands are also observed in the range of 430 nm, consistent with previous findings [26]. The N_2 spectrum (green) explicitly shows SPS bands from 300 to 400 nm, along with the First Positive System above 600 nm. The adamantane spectrum is absent near the UV region, but gradually appears towards the VIS region (300–400 nm), allowing for the possibility to observe the SPS bands when mixing adamantane with N_2. As helium is a monatomic gas, it lacks vibrational and rotational modes, thereby showing only distinct emission lines as shown in red. When mixed with adamantane, only a few He lines overlap with C_2 bands, with prominent peaks observed at 471, 491, 501, and 504 nm.

For a high-resolution spectral measurement, a SPEX 500 M monochromator was used to resolve the rovibrational structure of molecular spectra. Details on this setup are provided in [4], but will only be summarised here. A 3.5 mm diameter fused silica fibre optic cable is aligned with the centre of the discharge to collect the light from the plasma. The emitted photon efficiently propagates to the monochromator with a focal length of 500 mm, 1200 groove mm^{-1} grating, and adjustable slit width of up to 500 μm. The instrument captures the diffracted light with a ∼34 nm wavelength range and a ∼0.02 nm resolution for 15 μm slit entry. The SPEX MSD system controls a motorised grating adjustment to set the wavelength centre. The diffracted light is captured by an Ames Photonics Garry 3000S charge-coupled device array (3000 pixels) positioned horizontally at the monochromator's exit. It was noted that the measured intensity is slightly lower near both ends, so it is advisable to focus the wavelength range of interest within pixels 750–2250.

Significant RF interference affects the electronic signals, resulting in a low signal-to-noise ratio. To mitigate this issue, data preprocessing techniques, such as Savitzky–Golay or moving average filters, can be applied to smooth the data. However, filtering may obscure band heads, particularly at high rotational quantum number values. An alternative approach to reduce noise is background subtraction,

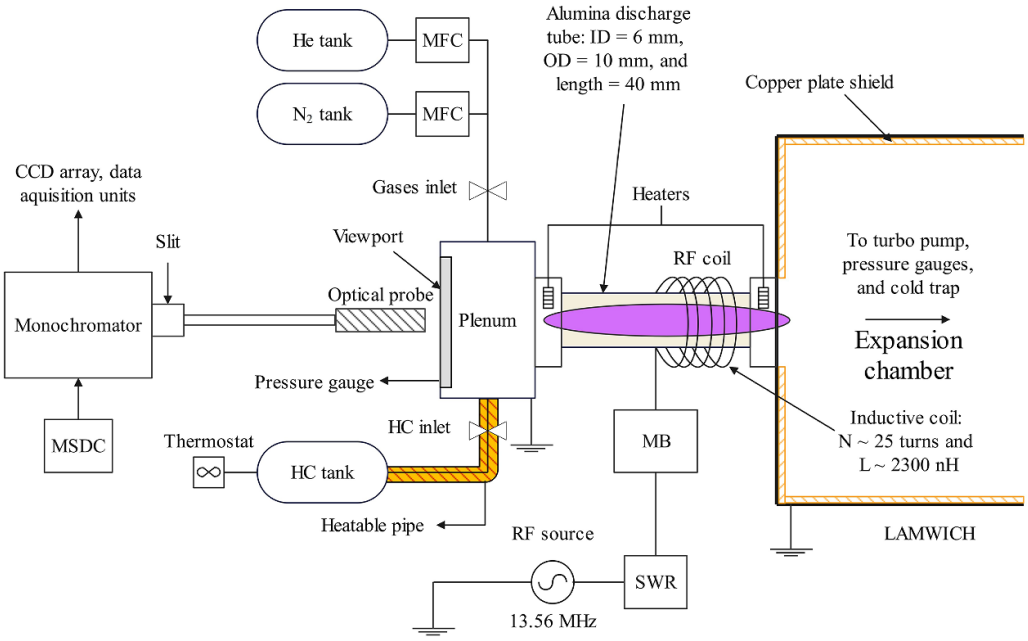

Figure 1. The schematic diagram of the experimental setup. The alumina discharge tube located at the centre is powered by an RF-generating system. Incoming gases and vapour flow from their original sources into an upstream plenum before passing through the discharge tube. Downstream, the flow expands into an expansion chamber housing the pumps, gauges, and a cold trap. The optical probe connected to the spectrometer is placed close to the viewport. Note that the diagram is not to scale.

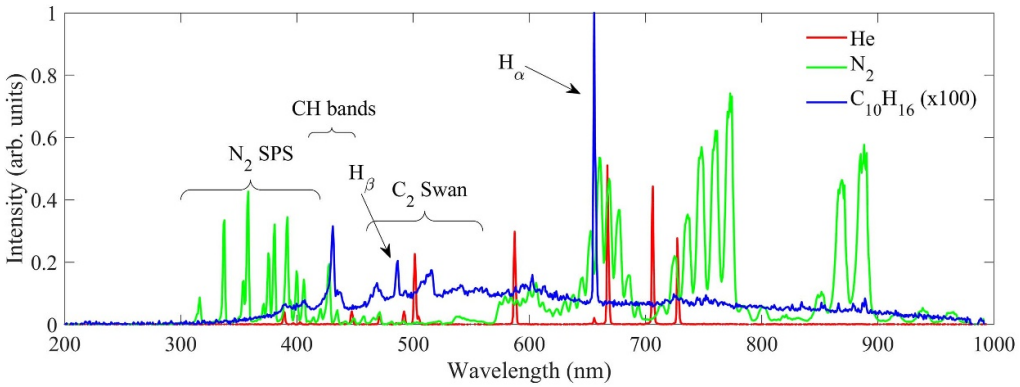

Figure 2. Overview emission spectra of He (——), N_2 (——), and $C_{10}H_{16}$ (——) using an Ocean Optics QE65000 spectrometer. Adamantane spectrum intensity is magnified by a factor of 100. Adamantane exhibits C_2 Swan bands covering from 460–560 nm, overlapping with He lines at 501.4 nm and a few weak N_2 bands. At 300–350 nm, N_2 displays SPS bands with minimal to no adamantane peaks in this region.

which involves capturing a background spectrum while the RF antenna is powered and then subtracting it from the measured spectrum.

3. Rovibrational bands fitting

In order to determine temperatures from rovibrational spectra, a good understanding of the electronic (n), vibrational (v) and rotational (J) quantum numbers is essential. Molecular emissions are produced by rovibronic transitions between two different states, each characterised by specific n, v, and J values. In the spectroscopic notation, a single prime ($'$) denotes quantities associated with the upper level, and double primes ($''$) indicate those appropriate to the lower level. Both N_2 SPS and C_2 Swan systems involve electronically allowed dipole transitions between two triplet states, represented as $^3\Pi$. In such transitions, the selection rule requires that the change in J follows $\Delta J = J' - J'' = -1$, 0, and 1, corresponding to P, Q, and R branches, respectively.

According to Planck's quantum jump concept, the wavenumber $\tilde{\nu}$ (or equivalently, frequency ν or wavelength λ) corresponding to the rovibronic transition can be derived from the total energy difference between two rovibronic states ($\Delta E^{n',v',J'}_{n'',v'',J''}$) [32].

$$\tilde{\nu} = \frac{1}{\lambda} = \frac{\nu}{c} = \frac{\Delta E^{n',v',J'}_{n'',v'',J''}}{hc} = (T'_e - T''_e) + (G' - G'') + (F' - F''), \quad (1)$$

where c is the speed of light in vacuum, h is Planck's constant, T_e, G, and F are the electronic, vibrational, and rotational energy in wavenumber units, respectively. Typically, $\tilde{\nu}$ is usually preferred over transition frequency (ν) and wavelength (λ) as the energy unit is in cm^{-1}; but for convenience, λ will be used in discussions, as it is more relevant to the VIS spectrum. While T_e is a constant value obtained from Huber's textbook [33] for both N_2 (pp. 418-420) and C_2 (pp. 112-114), G and F depend on v and J values, and can be calculated using molecular constants for a specific electronic state. Molecular constants of the SPS of N_2 are available in [34], while those for C_2 were initially reported in [35] and later updated in [36].

The general equation for calculating the theoretical emission spectra of both N_2 and C_2 was presented by Bai *et al* [11], initially introduced by Phillips [10] using the Dunham series [37], which is based on the molecular constants. In MassiveOES, theoretical emission spectra were modelled using a spectroscopic database. The transition frequency (ν) and Einstein coefficients ($A_{(v',J')\to(v'',J'')}$) for each rovibrational transition are related as shown in equation (2) [38],

$$A_{(v',J')\to(v'',J'')} = \frac{16\pi^3\nu^3 S_{J''}^{\Delta J}}{3\epsilon_0 hc^3\,(2J'+1)} \times \langle\psi_{(v',J')}|R_e(r)|\psi_{(v'',J'')}\rangle^2, \quad (2)$$

where ϵ_0 is the vacuum permittivity, $S_{J''}^{\Delta J}$ is the Hönl-London factor, and $\langle\psi_{(v',J')}|R_e(r)|\psi_{(v'',J'')}\rangle$ is the transition dipole moment (TDM) matrix. For C_2 Swan system, Hönl-London factors and TDMs were reported by Brooke *et al* [36] using PGOPHER program [39] by which TDMs were calculated by solving the one-dimensional Schrödinger equation to determine purely vibrational TDMs [40]. PGOPHER then used rotationaless TDMs as an input to calculate the rotational TDMs, which are being used to calculate the Einstein coefficients in equation (2). For N_2, the Einstein coefficients were reported in [8]. These A values are used to calculate the intensity of the spectrum as follows:

$$I_{v'',J''}^{v',J'} = \frac{(2J'+1)\exp\left(-\frac{E_{v'}}{k_B T_{vib}} - \frac{E_{J'}}{k_B T_{rot}}\right)}{Q(T_{vib},T_{rot})} A_{(v',J')\to(v'',J'')}, \quad (3)$$

$$Q(T_{vib},T_{rot}) = \sum_{v',J'}(2J'+1)\exp\left(-\frac{E_{v'}}{k_B T_{vib}} - \frac{E_{J'}}{k_B T_{rot}}\right), \quad (4)$$

where k_B is Boltzmann constant, T_{vib} and T_{rot} are the vibrational temperature and rotational temperature, respectively, $E_{v'}$ and $E_{J'}$ correspond to the energy in their particular mode, and $Q(T_{vib},T_{rot})$ is the partition function for assumed independent vibrational and rotational states. The fine structure splitting effect due to Λ-type doubling is already taken into account for $E_{J'}$. In MassiveOES, $E_{v'}$ value already included the electronic energy T_e. The observable J values extend only up to 30, which is sufficient to determine the rotational temperature. Under certain conditions, higher J levels have been reported to exhibit rotational-translational non-equilibrium [41]. Furthermore, Davis and Gottscho [6] validated the reliability of gas temperature measurements using $J<23$ through laser-induced fluorescence (LIF) methods.

Although several studies have suggested that Gaussian fitting is adequate for matching experimental and theoretical spectra [4, 10], this work uses the Voigt profile to simulate spectra. The Voigt profile, a convolution of Gaussian and Lorentzian functions, accounts for Doppler broadening as well as natural and collisional broadening, respectively [42].

$$V(\lambda;\sigma,\gamma) = \int G(\lambda;\sigma)\,L(\lambda-\lambda';\gamma)\mathrm{d}\lambda', \quad (5)$$

where $G(\lambda;\sigma)$ is the Gaussian function with standard deviation σ and, λ' is the wavelength at which the Gaussian component is centred, and $L(\lambda-\lambda';\gamma)$ is the Lorentzian function with a half-width at half-maximum γ. The wavelength calibration was corrected by a quadratic equation. The simulated spectra are computed using the least-squared fitting method with at least 50 000 iterations. In this work, the errors derive from a combination of non-systematic and systematic sources. Non-systematic errors arise from repeated measurements, while systematic errors are due to discrepancies in the rovibrational band fitting. These errors are presented as error bars in the temperature plots presented later.

The current study encountered several limitations. One major issue was the unavoidable RF noise interference from the RF antenna, which affected the spectral results and reduced the signal-to-noise ratio. Additionally, the spatial effects on the rotational temperature were not considered, as the size of the optical probe was comparable to the discharge diameter, limiting spatial resolution. Furthermore, temporal changes in the spectra could not be investigated due to the need for consistent acquisition times across varying experimental conditions, preventing a detailed analysis of time-dependent behaviour.

4. Results and discussion

4.1. Validation of rovibrational band fitting for pure N_2 plasma

Although many have shown that the rotational temperature of N_2 rovibrational spectra can serve as a reasonable estimate for neutral gas temperature [4, 5, 7, 11, 20], it is worth performing such measurements under the experimental conditions of this study. Four series of SPS bands ($\Delta v = +1, 0, -1, -2$) were measured using a SPEX 500 M monochromator and fitted using MassiveOES software as illustrated in figures 3(a)–(f). The best-fit spectra (in red) were obtained through a least-squares method as shown in panels (a)–(d). These fitted spectra were used to determine T_{vib} and T_{rot} from equation (3), with results as a function of RF power presented in figures 3(e) and (f). By adding several tens of watts, T_{rot} reaches a few hundred Kelvin whilst T_{vib} is around a few thousand Kelvin. As expected, T_{vib} is approximately an order of magnitude higher than T_{rot}, highlighting that the vibrational mode of excited N_2 molecules is not in equilibrium with the rotational mode, as previously observed [7, 11].

As RF power increases, both T_{vib} and T_{rot} show a steady rise. The behaviour of T_{rot} has been previously observed by

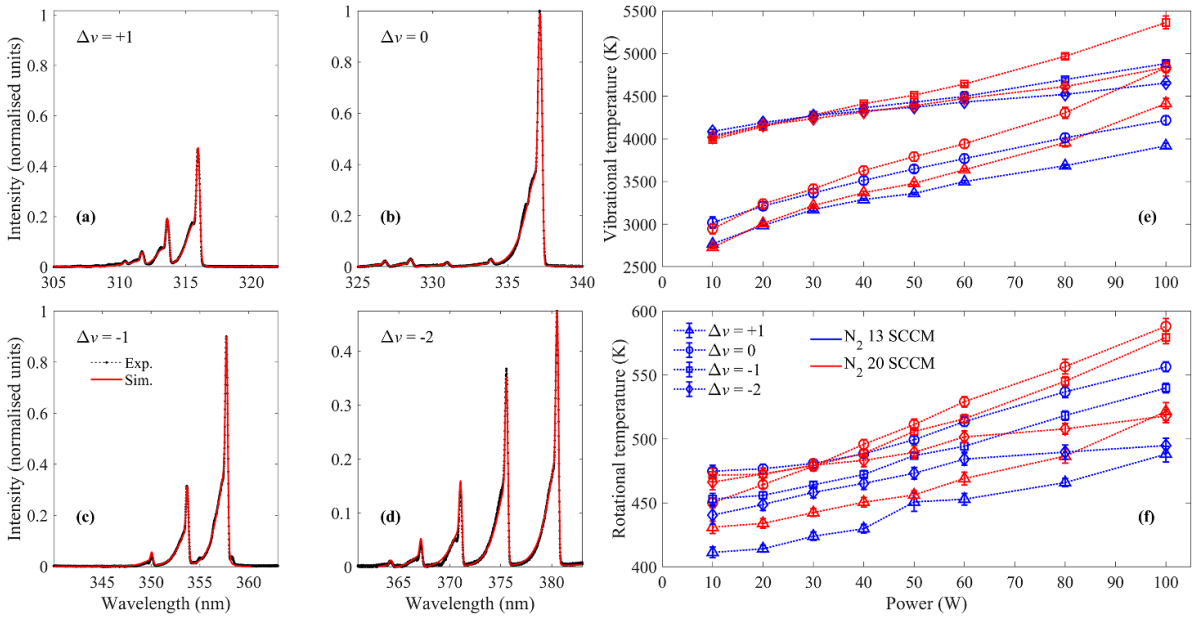

Figure 3. (a)–(d) Examples of experimental (— · —) and simulated (——) spectral fits for pure N_2 plasma at 20 SCCM and 60 W, showing different vibrational bands for $\Delta v = +1$, 0, -1, and -2, respectively. (e) and (f) Vibrational and rotational temperatures plotted as a function of RF power for each vibrational band: $\Delta v = +1$(△), 0 (◯), -1 (×), and -2 (✳) across two different flow rates: 13 SCCM (——) and 20 SCCM (——). Intensities in (a)–(d) are normalised with respect to (0,0) SPS band head. The error bar in (e) and (f) represents the combined values of the standard deviation of multiple measurements and systematic errors.

Karakas *et al* [12] and is likely attributed to a higher electron density (n_e) which induces increasing ionisation and molecule excitation. Meanwhile, the trend of T_{vib} with increasing input power is consistent with findings from other studies [4, 7]. Figures 3(e) and (f) also shows observations for flow rates of 13 SCCM (blue solid line) and 20 SCCM (red solid line), corresponding to measured plenum pressures of 0.25 and 0.32 Torr, respectively. A higher flow rate—or higher pressure—leads to increased temperatures due to the higher neutral gas density (n_g) within the discharge. The elevated n_g increases collision frequencies across all interaction types: neutral-neutral collisions raise the gas temperature, neutral-electron collisions enhance excitation and ionisation, and ion-neutral collisions increase charge exchange. This increase in collision rates enhances the likelihood of energy transfer to vibrational and rotational modes, leading to higher T_{vib} and T_{rot}, consistent with findings of Zhang *et al* [7].

In the upper right panel figure 3(e), two separated T_{vib} values of ∼3000 K for $\Delta v = +1$ and 0 and ∼4000 K for $\Delta v = -1$ and -2, begin to divert further as input power increases. These observations agreed well with those reported in [7]. In the lower right panel figure 3(f), T_{rot} gradually increases from 410 to 580 K over RF power, aligning with measurements obtained via OES under similar experimental conditions and supported by the I-N CEX power balance model [4]. A rotational temperature of ∼450 K for pure N_2 at 10 W is consistent with the neutral gas temperature predicted by the neutral gas heating mechanism model [4], affirming the reliability of using rotational temperature as a gas temperature estimate. The deviation in T_{rot} is ∼50 K, comparable to a previously reported deviation of ∼40 K across all studied bands [7], suggesting consistent rotational temperatures among the different vibrational bands. In this study, the $\Delta v = 0$ band was chosen as the $\Delta v = -1$ and -2 bands can overlap with weak emissions from adamantane starting around 350 nm, as seen in figure 2. The $\Delta v = +1$ band was not considered due to poorer spectral fit quality, which resulted in underestimated T_{rot} values. Furthermore, its lower intensity compared to $\Delta v = 0$ makes it challenging to resolve when the nitrogen is present only in trace amounts, see figures 3(a) and (b).

4.2. Justifications of using trace amount of N_2 in an adamantane plasma

The next step involves determining the vibrational and rotational temperatures of adamantane with a trace amount of N_2. Figure 4 shows the spectral fit for the SPS $\Delta v = 0$ band series and corresponding temperatures for a plasma generated from 2.47 SCCM (equivalent to 0.25 mg s^{-1}) of adamantane with 5% N_2 (equivalent to 0.1 SCCM N_2) at 60 W RF power. In this case, the estimated plenum pressure was ∼80 mTorr, with the discharge pressure halved according to choked flow at the discharge exit [43]. It was found that obtaining measurable spectra from this mixture was challenging, likely because adamantane, the primary species in the discharge, undergoes extensive dissociation rather than ionisation or excitation, resulting in lower emission intensity. The slit width was therefore increased to capture more photons. T_{vib} and T_{rot} were confirmed to remain relatively unaffected by the slit width adjustment, as noted by [7]. The accuracy the fit, assessed via Chi-square value (χ^2), was slightly higher for the adamantane-N_2 mixture compared to pure N_2, potentially due to a small,

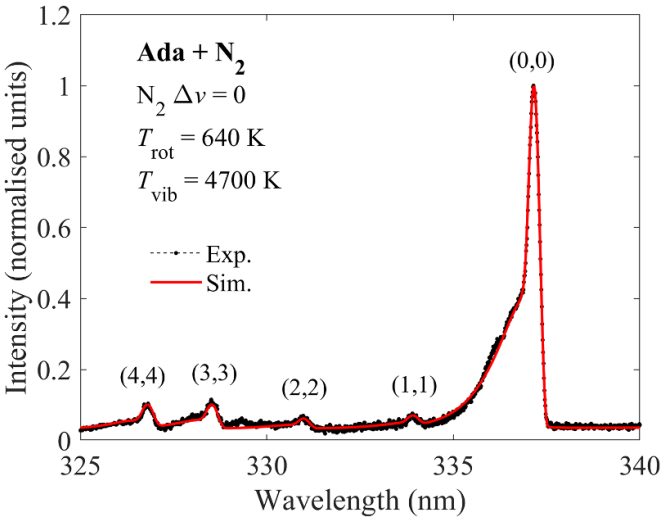

Figure 4. Examples of experimental (— · —) and simulated (——) spectral fit of N_2 SPS $\Delta v = 0$ series for 2.47 SCCM adamantane (equivalent to 0.25 mg s^{-1}) with 5% N_2 (equivalent to 0.1 SCCM N_2) at 60 W RF power, showing $T_{rot} = 620$ K and $T_{vib} = 4600$ K. Due to weak light emission, the entrance slit was widened to 200 μm to improve light collection for this case. Vibrational transitions (X', X'') are labelled at each band head, with X denoting the vibrational state.

unidentified peak likely arising from adamantane fragments at ~329 nm, as shown in figure 4. Nonetheless, the overall fit for the (0,0), (1,1), (2,2), (3,3), and (4,4) bands was satisfactory.

In high-pressure pure N_2 discharges, the rotational temperature typically is in thermal equilibrium with the neutral gas temperature. However, this equivalence does not necessarily hold in gas mixtures. To equate the rotational temperature of the excited state of the SPS (N_2(C)) with the host gas temperature (T_g), certain conditions must be satisfied. This study adopts flow conditions based on Wang *et al* [19]. The first condition is that the effective lifetime of N_2(C) (τ_{eff}) must be greater than the rotational energy transfer (RET) relaxation time (τ_{RET}) such that thermalisation between rotation and translation can be achieved before the radiative decay of N_2(C).

Given that the radiative lifetime (τ_{rad}) of N_2(C) is ~40 ns for $v = 0$ level under vacuum conditions [44], τ_{eff} may be faster due to the collisional quenching effect. Under the current experimental conditions, the effective lifetime of N_2(C) can be expressed as $\tau_{eff}^{-1} = \tau_{rad}^{-1} + \tau_{Q,tot}^{-1}$, where $\tau_{Q,tot^{-1}}$ is the total quenching rate from collisions with electrons, adamantane, and N_2. Since this setup is similar to the capacitively coupled plasma (CCP) discharge [3], the plasma is weakly ionised (<1%), leading to a predicted electron temperature (T_e) and plasma density (n_e) of ~3 eV and ~10^{12} cm^{-3}, respectively. The plasma density is derived based on 1% fractional ionisation and the ideal gas law (see more detail in the Supplementary Material). Given an electron quenching cross-section of ~10^{-15} cm^2 [19], the electron quenching rate is on the order of ~10^5 s^{-1}. In low-temperature plasmas (T_e <10 eV and low power density <15 W cm^{-3}), adamantane fragments are assumed to be in negligible quantities [25], and hence the predominant quencher is adamantane. Although data for the quenching rate constant of adamantane ($k_{q,ada}$) is unavailable, it is assumed to be ~10^{-10} cm^3 s^{-1}, a typical value for similar quenchers [5], resulting in a quenching rate of N_2(C) by adamantane comparable to that by electrons. The quenching effect of trace N_2 is minimal due to its low concentration and low quenching rate constant. In total, the total quenching rates are about two orders of magnitude lower than the τ_{rad}, causing a τ_{eff} very close to τ_{rad}. Since RET data for N_2(C) state with adamantane could not be found, a comparable RET rate constant (k_{RET}) of ~10^{-10} cm^3 s^{-1}, based on experimentally studied collision partners, is assumed [5]. This yields an estimated τ_{RET} of ~10 μs. From this analysis, τ_{RET} is an order of magnitude slower than τ_{eff}. Therefore, the first condition is unmet, consequently leading to the consideration of the second condition.

The second condition states that the gas temperature (T_g) can be approximately equal to T_{rot} of nitrogen ground state (N_2(X)) if direct electron impact excitation from N_2(X) is the dominant production mechanism rather than excitation from metastable states of adamantane as a host gas. Considering a production of N_2(C) state can be mainly generated from either its ground state in equation (6) or its metastable state (N_2(A)) in equation (7):

$$N_2(X) + e \rightarrow N_2(C) + e, \quad (6)$$

$$N_2(A) + e \rightarrow N_2(C) + e. \quad (7)$$

Despite the reported electron excitation rate constants for N_2(A) are at least two orders of magnitude higher than those for N_2(X) [5], Benedictis and Dilecce experimentally demonstrated that the excitation from N_2(X) is the dominant process in N_2 discharges at pressures around a few Torr [45]. Consequently, this work has ignored equation (7). In equation (6), the electron excitation rate for T_e ~3 eV yields 2.7×10^{-10} cm^3 s^{-1} [5], resulting in a rate of ~10^4 s^{-1}. Since only 1% of adamantane is ionised and less than 1% is fragmented in the discharge, the adamantane ion ($C_{10}H_{16}^+$) is assumed to behave as a metastable species. With a calculated adamantane ion density of ~10^{13} cm^{-3}), a metastable excitation rate resulting from adamantane ion of ~10^3 s^{-1} is derived using a typical metastable excitation rate constant of ~10^{-10} cm^3 s^{-1} [5]. Even though substantial adamantane fragments may be present, all possess internal energies below 10 eV [25], which is insufficient for exciting N_2(X) of 11 eV. Therefore, this condition is reasonably justified. Given that the rotational constant (B_e) of N_2(X) ($B_e = 2.010$ cm^{-1}) and N_2(C) ($B_e = 1.826$ cm^{-1}) are nearly the identical [32] (pp. 552–553), supporting the assumption that rotational temperatures of the excited and ground states are in equilibrium or $T_{rot}(X) \approx T_{rot}(C)$ [19].

Although the estimated pressure in the adamantane-N_2 plasma is approximately a third of that in pure N_2, the measured T_{rot} and T_{vib} increased from 520 and 3700 to 640 and 4700 K, respectively. This rise is likely due to excess energy released during the dissociation of adamantane, which redistributes across various degrees of freedom, particularly,

in rotational and vibrational modes. A similar temperature increase associated with dissociation energy has been observed via N_2 (0,0) band when the gas temperature changed from 800 K in Ar plasma to 1100 K in chlorine (Cl_2) plasma under the same conditions of a few mTorr pressure and ∼500 W RF power [9]. Further studies of the gas temperature measurements in carbon-based complex plasma mixtures, such as CCl_4 [6], CH_3F/O_2 [12], buffer gas/C_2F_6/C_4F_8 [46], and C_2F_6/O_2/Ar [11], have also been conducted using SPS bands.

4.3. Justifications of using C_2 Swan band in an adamantane plasma

Since C_2 molecules can form through the dissociation of adamantane, adamantane alone can exhibit C_2 Swan system. An attempt was made to resolve the C_2 spectra from pure adamantane plasma; however, the signal-to-noise ratio was too low to reliably determine the rotational temperature through band fitting. The reason is that adamantane possesses multiple rotational and vibrational degrees of freedom, allowing the energy to be absorbed into its rotational and vibrational modes, which typically releases energy in the near IR [24] or VUV [25] rather than VIS range. Furthermore, adamantane undergoes dissociation, producing molecular fragments that interfere with the C_2 spectra. To compensate for these effects, this work proposes adding a buffer gas to increase the electronic excitation population from ionised high-energy electrons. While Ar has been commonly used in similar studies [11, 26], the present work found multiple Ar II lines between 510–515 nm overlapped with the C_2 $\Delta v = 0$ region. As a result, helium was used instead.

Figure 5 displays emission spectra in the 500–530 nm range for 84 SCCM pure He plasma (red) and 2.47 SCCM adamantane + 84 SCCM He plasma (blue) with a 20 ms acquisition time (top panel) and 5 s acquisition time (top panel). Noting that adamatane-He mixture plasma could not be sustained with a He flow rate below 80 SCCM in this RF power range, possibly due to the strong electronic configuration of He (e.g. ionisation threshold of ∼24.6 eV). In this figure, it can be seen that He emission lines do not interfere with the targeted C_2 $\Delta v = 0$ heads which occupies between 506 and 516 nm with rotationally resolved features. Two aspects can be drawn from these diagrams: first, the emission intensity of C_2 (0,0) band head (at ∼516 nm) is three orders of magnitude weaker than the two He I lines of 501.5 nm and 504.7 nm, as illustrated in the magnified view in the top pane. This intensity corresponds to a normalised intensity of ∼1 in the bottom panel, where the acquisition time is 1000 times longer than in the top. The long acquisition time in the lower pane leads to saturation of the He lines due to the instrument's light capture limits. Second, the upper pane shows that the addition of adamantane enhances the He I line at 501.5 nm, corresponding to the ^1S—$^1P^o$ transition, by ∼13% while the He I line at 504.7 nm remains unchanged, consistent with observations from He-methane/butane microwave discharge experiments [47]. A faint band around 520 nm is likely a (0,2)

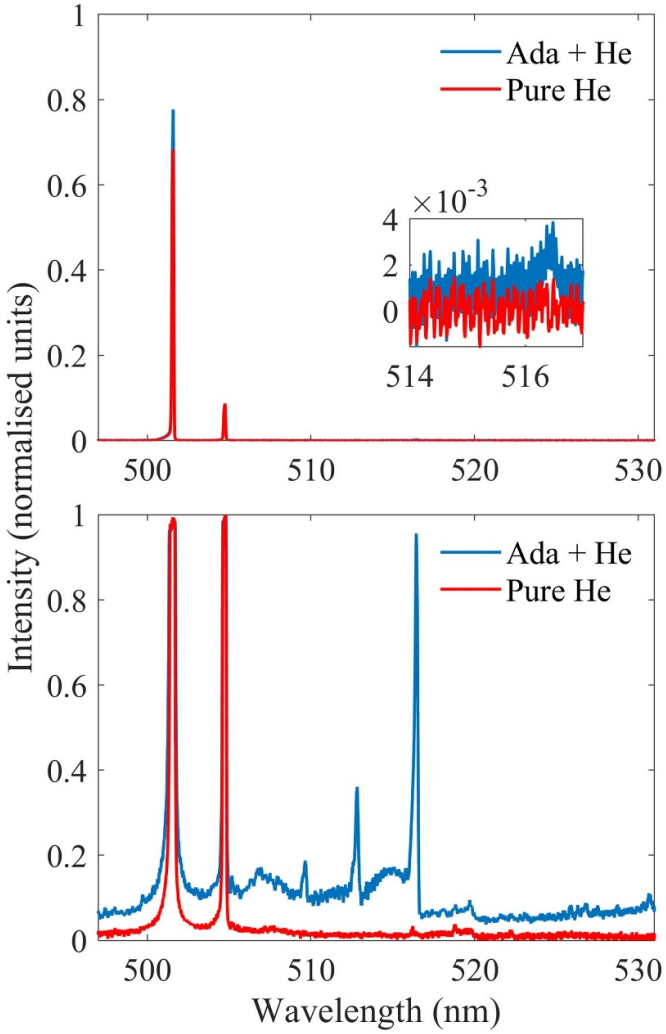

Figure 5. Comparison of the emission spectra for an adamantane-helium mixture (——) and pure helium (——) in the 500–530 nm range with acquisition times of 20 ms (top) and 5 s (bottom). The top panel includes a magnified view of the 514–516 nm region. The observed intensity of the (0,0) C_2 band head is three orders of magnitude lower than that of the He emission lines.

CO Angström band, resulting from the impurity of the discharge. This interference, combined with the broadening of the He I line at 504.7 nm, led to the selection of rovibrational band fit for the (0,0), (1,1), and (2,2) C_2 $\Delta v = 0$ transitions, which are situated between 508 and 518 nm.

Figure 6 shows the spectral fit for the Swan $\Delta v = 0$ transition and the corresponding temperatures for a plasma generated from 2.47 SCCM adamantane (equivalent to 0.25 mg s^{-1}) and 168 SCCM He (equivalent to 0.5 mg s^{-1}), at the same RF power as the adamantane plasma with trace amount of N_2 shown in figure 4. Compared to the results from the SPS $\Delta v = 0$ transition, the estimated plenum pressure was about an order of magnitude higher than in previous cases (∼1 Torr). As expected, T_{rot} was 450 K, slightly lower than the temperature measured in the N_2 spectra, likely because He, the primary gas in the discharge, has high thermal conductivity and a higher flow rate, resulting in rapid gas cooling [19].

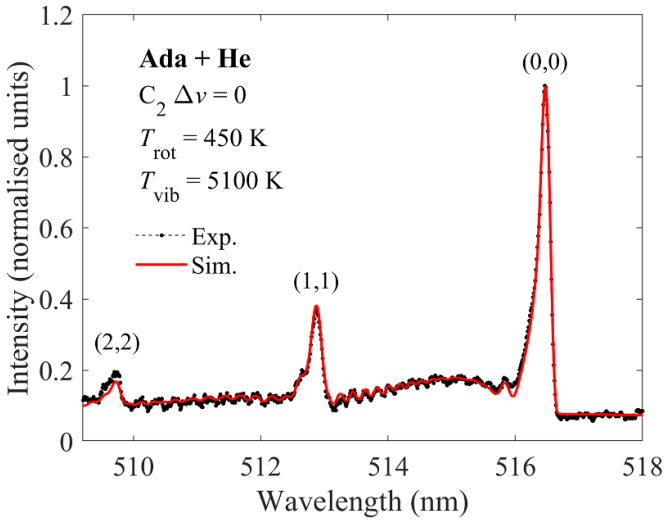

Figure 6. Examples of experimental (— · —) and simulated (——) spectral fit of C_2 Swan $\Delta v = 0$ series for 2.47 SCCM adamantane (equivalent to 0.25 mg s^{-1}) with 168 SCCM He (equivalent to 0.5 mg s^{-1}) at 60 W RF power, showing $T_{rot} = 450$ K and $T_{vib} = 5100$ K. Vibrational transitions (X', X'') are labelled at each band head, with X denoting the vibrational state.

Table 1. Radiative life time (τ_{rad}) and rotational relaxation rate (k_{RET}) of the C_2(d) state reported by several authors.

Reporter(s)	τ_{rad}	k_{RET}	Pressure	Reference
Setser *et al*	200 ns	7.14×10^{-12} cm^3 s^{-1}	0.5–80 Torr	[50]
Brockhinke *et al*	0.28–1.5 ns	1.25×10^{-12} cm^3 s^{-1}	1 atm	[17]
Erman	120 ns	6×10^{-11} cm^3 mol^{-1} s^{-1}	∼1 mTorr	[51]

A similar decrease in gas temperature was discovered in the sputter etching of C_2F_4 with added He [48]. On the contrary, T_{vib} increased to 5100 K, potentially resulting from the relatively slow vibrational relaxation of the excited state of Swan (C_2(d)) (slower than rotational relaxation), allowing molecules to remain in vibrationally excited longer, as reported by [49].

Using a similar analysis to the previous case, the radiative lifetime and thermalisation time were estimated for the C_2(d) state. Various studies have reported different values for k_{RET} and τ_{rad} for C_2(d), see table 1. The collected data reported by Setser *et al* was selected for this analysis due to its comparable operating pressure of ∼0.5 Torr. Here, He is the major quenching species, thereby neglecting the electronic and hydrocarbon quenching. Assuming a quenching rate of C_2(d) by He similar to that of N_2(C), $R_{q,He} \sim 10^7$ s^{-1} [5], yielding $R_{Q,tot}$ very close to $\sim 1.5 \times 10^7$ s^{-1}. With k_{RET} equal to 7.14×10^{-12} cm^3 s^{-1}, the resulting τ_{RET} is 9.3 μs, significantly slower than τ_{eff}, indicating that the first condition is, once again, unmet.

Although no work has specifically reported on the production mechanisms of the electronically excited C_2(d) state from adamantane, there are three possible mechanisms that could form the C_2(d) state: the formation of two ground-state carbon atoms (^{3}P) [16], dissociation of adamantane fragments, and electron impact excitations from the C_2 ground state (C_2(X)), represented by the following reactions:

$$C\left(^3P\right) + C\left(^3P\right) + M \rightarrow C_2\left(d\right) + M, \quad (8)$$

$$C_xH_y\left(x \geqslant 2, y \geqslant 0\right) + M \rightarrow C_2\left(d\right) + C_{x-2}H_y + M, \quad (9)$$

$$C_2\left(X\right) + e \rightarrow C_2\left(d\right) + e, \quad (10)$$

where C_xH_y represents any adamantane fragment with $x \geqslant 2$ and $y \geqslant 0$, M is the third body particle stabilising the transition state, and $C_{x-2}H_y$ is the fragment daughters. As no information can be found for such reactions, the justification can not be qualitatively comprehended. This work assumes thermal equilibrium based on the detailed description provided by Wang *et al* [19] and previous observations in low-pressure plasma [9]. Studies on gas temperature using Swan band emission spectroscopy in plasma mixtures such as CO_2 [16], CF_4/Ar and CH_4/CO_2 [18], C_2F_6/O_2/Ar [11], CH_4/H_2/Ar [14], ($\leqslant$ 6%)CH_4/H_2 [52] and CF_4 [15], have demonstrated the reliability of using this thermalisation approach.

4.4. Study of adamantane plasma with trace N_2: variations in N_2 contents, RF Power, and adamantane mass flow rate

In this section, adamantane plasma trace N_2 characterisation was comprehensively studied. Figure 7(a) shows the rotational/gas temperature of adamantane plasma as a function of RF power with varying N_2 concentrations, while figure 7(b) shows the emission intensity of the (0,0) SPS band head under the same conditions. The temperature is found to be a fairly linear relationship with power regardless of the N_2 concentration, consistent with the previous demonstrations in figure 3. To minimise the influence of the probing gas, many studies have used less than 1% N_2 to determine the gas temperature of a main gas [4, 19]. However, a typical range of 2–5% is recommended by the literature for working gases containing carbon-based molecules [9, 11, 12]. This recommendation stems from

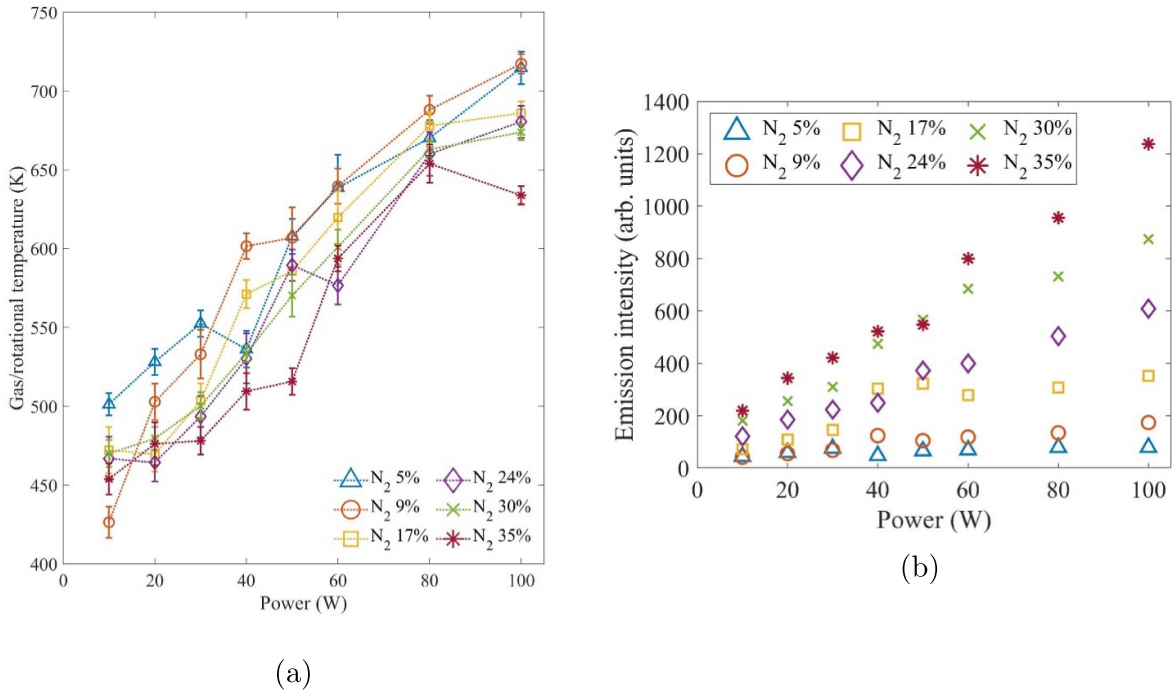

Figure 7. (a) Gas/rotational temperature and (b) emission intensity of the (0,0) SPS band head, as a function of RF power measured for several N_2 contents: 5% (△), 9% (○), 17% (□), 24% (◇), 30% (×), and 35% (✳). The error bar represents the combined values of the standard deviation of multiple measurements and systematic errors.

the fact that most carbon-based molecules tend to produce very weak emission intensities. This ensures an adequate spectral signal for reliable measurements.

The effect of N_2 concentration on temperature can be presumably difficult to interpret. To the best of our knowledge, the observed trend shows a decrease in temperature with increasing N_2 content, with variations of ∼80 K. This contrasts with Ar-N_2 ICP plasma where the concentration typically has minimal [20] or proportional impact on temperature [21]. Britun *et al* further suggested that temperature can be significantly influenced by coupling mode, where temperature rapidly rises as the plasma transitions from capacitive (E-mode) to inductive (H-mode) coupling [20]. To investigate this, the emission intensity of the (0,0) SPS band head at various N_2 content was plotted against RF power to observe any intensity jumps associated with coupling transitions, as shown in figure 7(b). At lower N_2 contents (<10%), the emission intensity remains relatively constant across the RF power range. For higher N_2 contents, the intensity slowly increases from 10 to 50 W, then sharply rises beyond 50 W. A pronounced intensity jump from 50 to 60 W, observed with 35% N_2 addition, was envisaged to be the E-H mode transition, likely explaining the rapid temperature increase in figure 7(a). This coupling transition power aligns well with the previous experiments conducted at similar conditions but with an RF frequency of 40.68 MHz [53]. However, higher N_2 concentrations alter plasma conditions, potentially compromising the accuracy of gas temperature measurements intended to represent pure adamantane plasma. Therefore, 5% N_2 was used to reliably diagnose the plasma.

Figure 8 shows the rotational/gas temperature and the emission intensity as a function of an RF power for adamantane with 5% N_2 plasma at various adamantane mass flow rates. With N_2 flow fixed at 5% of total flow, only E-mode coupling occurred in the discharge. As expected, the temperature increases with RF power for all adamantane mass flow rates. In Ar plasma, gas heating is typically driven by I-N CEX mechanisms [3, 4] or electron pressure [53]. In molecular plasma, the source of neutral heating appears to stem from the dissociation and dissociative ionisation [11]. The observed 200 K increase between 10 and 100 W, compared to pure N_2 plasma, is likely due to the exothermic dissociation reactions of adamantane. With higher adamantane flow rates, T_g generally increases, except for 0.25 mg s^{-1}. Higher flow rates imply increased collisions, enhancing dissociation rates, as discussed in section 4.1.

In contrast, the 0.25 mg s^{-1} adamantane shows a distinct trend, resulting in the highest temperature from 10–30 W, levelling off at 40 W, then rising again with power. The cause of this anomaly is still unclear, but one possible reason is that the emission intensity for this flow rate is relatively low compared to other rates (see figure 8(b)). The intensity suddenly decreases at 40 W and then slightly increases with a higher power, matching the temperature trend and suggesting unidentified processes in this region. A similar intensity dip is weakly observed at 40–50 W for other flow rates. Notably, the

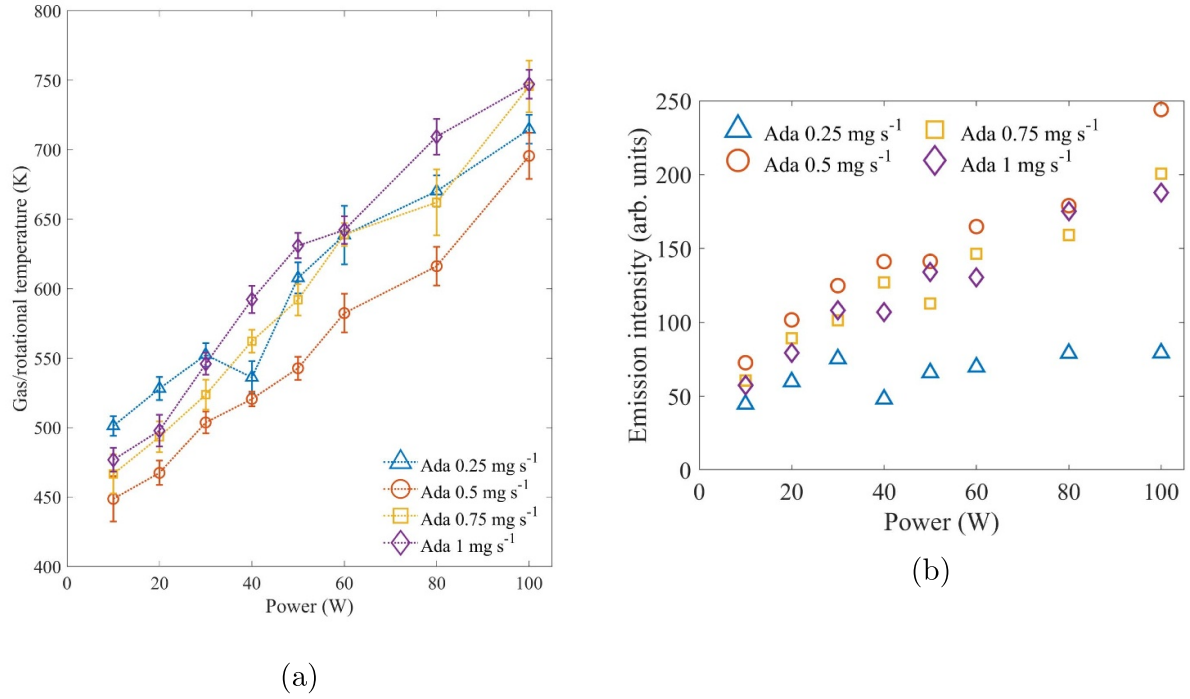

Figure 8. (a) Gas/rotational temperature and (b) emission intensity of the (0,0) SPS band head as a function of an RF power for adamantane with 5% N_2 plasma measured in several mass flow rate of adamantane: 0.25 mg s^{-1} (△), 0.5 mg s^{-1} (○), 0.75 mg s^{-1} (□), and 1 mg s^{-1} (◇). The error bar represents the combined values of the standard deviation of multiple measurements and systematic errors.

matching network was retuned in this region, as power changes began to affect reflected power, potentially indicating a subtle coupling mode transition. Further investigation, such as mass spectrometry or electric diagnostics, is necessary to determine any significant changes in resident species or plasma density.

The following calculations are based on the power balance model (assuming a Maxwellian distribution) introduced by Bai *et al* [11] to verify the result obtained by optical spectroscopy. For the case of 0.25 mg s^{-1} adamantane at 10 W RF power, yielding T_g of ∼500 K, the input power (P_{in}) is dissipated through four main channels: dissociation of adamantane (P_{diss}), ion creation/loss through plasma sheath to the wall ($P_{i,loss}$), conduction from the discharge gas through the wall (P_{cond}), and convection through the downstream (P_{conv}) as derived below. It is important to note that plasma conduction is defined as a thermal energy transfer through the conductive plasma state.

$$P_{in} = P_{diss} + P_{i,loss} + P_{cond} + P_{conv}, \quad (11)$$

$$P_{i,loss} = \exp(-0.5) A_s n_e v_B \langle \epsilon_{loss} \rangle, \quad (12)$$

$$P_{cond} = K \frac{T_g - T_w}{L_{eff}} A_s, \quad (13)$$

$$P_{conv} = \dot{m} C_p (T_g - T_f). \quad (14)$$

where A_s is the plasma wall surface area, v_B is Bohm's velocity ($v_B = (eT_e/M)^{1/2}$), $\langle \epsilon_{loss} \rangle$ is the average energy loss per ion, K is the thermal conductivity of the plasma assuming to be ∼70 mW m^{-1} K^{-1} based on available data of hydrocarbons (e.g. methane or propane at 500 K), L_{eff} is the characteristic length assuming to be a discharge radius of 3 mm, $\dot{m}$ is adamantane mass flow rate, C_p is the heat capacity at a constant pressure of adamantane vapour assuming to be ∼3 kJ kg^{-1} K^{-1} obtained from the same data source as k, and T_w and T_f are the wall and gas inlet temperatures, respectively, both set to 325 K.

Assuming 1% of adamantane is completely dissociated, P_{diss} can be calculated from the total energy required to break all bonds in $C_{10}H_{16}$. This comprises of 12 C–C bonds (346 kJ mol^{-1} per bond) and 16 C–H bonds (420 kJ mol^{-1} per bond). The resulting P_{diss} is ∼0.2 W, equivalent to 2% of the total input power, contrasting with previous results (∼30%) observed in high power density plasma [11]. $\langle \epsilon_{loss} \rangle$ is assumed to be the sum of the ionisation threshold of adamantane (9.3 eV [25]) and the average sheath voltage (an experimental value of 20 V based on atomic plasma [3], doubled to 40 V for molecular plasma due to higher collisional losses through dissociation, rotational, and vibrational modes [54]), yielding ∼50 eV. The calculated $P_{i,loss}$ is 5.3 W, about half of the input power, agreeing well with the previous report under comparable discharge pressure and power conditions [7]. P_{cond} and P_{conv} are estimated to be 1.9 W and 0.13 W, respectively. A convection dissipation of less than 1% is considered negligible in power distribution, consistent with previous work [7, 11]. The conduction term, however, is significant, accounting for about 20% of the total power dissipation, similar to spatial power distribution observations in Ar micro-discharge plasmas [3, 55]. About 20% of input power was dissipated via conduction through the wall, resembling the previous study [7, 11]. These losses amount to ∼75%

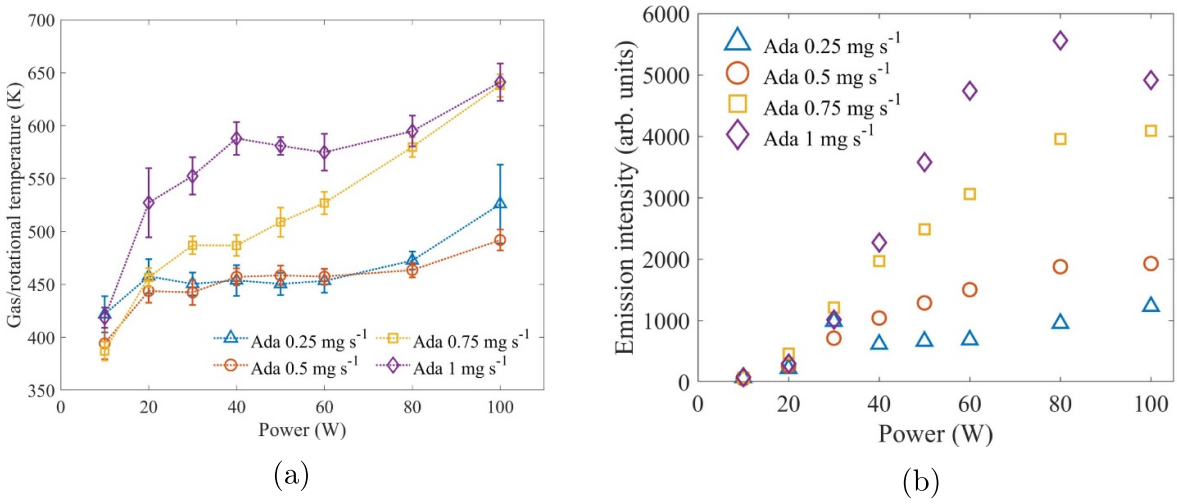

Figure 9. (a) Gas/rotational temperature and (b) emission intensity of the (0,0) Swan band head as a function of an RF power for adamantane with 168 SCCM He plasma measured in several mass flow rate of adamantane: 0.25 mg s^{-1} (△), 0.5 mg s^{-1} (○), 0.75 mg s^{-1} (□), and 1 mg s^{-1} (◇). The error bar represents the combined values of the standard deviation of multiple measurements and systematic errors.

of the input power, suggesting an underestimate of the loss of dissociation power, as prior studies have reported a dissipation proportion similar to the ion creation/loss term. Bai *et al* [11] calculated the dissociation energy that accounted for almost 30% of the total energy. Similarly, Zhang *et al* [7] examined highly constricted N_2 plasma and estimated that the dissociation energy of N_2 constituted ∼40%, based on the dissociation degrees of 2–15%. Power balance calculations at higher RF power were not pursued due to limited data for those conditions.

4.5. Study of adamantane plasma with helium buffer: variations in RF power, adamantane mass flow rate, and discharge pressure

Although introducing large amounts of helium may alter the plasma behaviour of adamantane, which is the primary interest, these results can be useful for plasma processing applications, such as nanodiamond synthesis [26, 56]. Figures 9(a) and (b) present the rotational/gas temperature and the emission intensity of the (0,0) Swan band head, respectively, as a function of an RF power for adamantane with a fixed 168 SCCM He flow and varying adamantane mass flow rates. As expected, gas temperature increases with RF power and adamantane flow, similar to the trends observed in section 4.4. Interestingly, the temperature mutually starts ∼400 K at 10 W for all mass flow rates and stabilises ∼450 K between 30 and 80 W for the flow rates under 0.5 mg s^{-1}. For higher flow rates, this mid-range stability diminishes, with the temperature gradually rising to ∼650 K at 100 W. This unusual behaviour in the adamantane-He mixture likely indicates that rotational excited C_2 molecules have already reached saturation, limiting further energy absorption, so the excess energy is instead distributed to other species, as evidenced by increased He I intensity when adamantane is added, see figure 5. In addition, this saturation is also reflected in the measured T_{vib}, which remains stable across mid-range RF power. The emission intensity, as shown in figure 9(b), remains nearly constant across all power levels, suggesting low production of C_2 species. However, higher adamantane flow rates show a sharp increase in intensity with increasing power, followed by a recession at 100 W. The similar parabolic shape of (0,0) Swan intensity (without downturn) was previously observed in the LIF measurement [17]. While the reason for the drop at 100 W remains unclear, it could be due to rapid changes in chemical reactions affecting the distribution of fragmented species.

To determine whether helium contributes to the constant gas temperature at the mid-range RF power, an additional study of gas temperature and emission intensity in a He with 5% N_2 plasma using (0,0) SPS band fit was performed, as shown in figures 10(a) and (b), respectively. Two observations can be made from these measurements: one, no stable gas temperature is observed, suggesting that this unusual behaviour is likely due to adamantane reactions rather than He. Second, the large amount of He of (up to 1 mg s^{-1}, corresponding to a 336 SCCM) introduces significant collisional quenching with N_2, as detailed in [41], reducing the gas temperature by ∼50 K compared to pure N_2 plasma (see section 4.1). Unlike the C_2 intensity, the SPS emission intensity for all cases follows a similar increasing trend, with higher He flows yielding slightly higher intensity as illustrated in figure 10(b). This outcome is reasonable, as the fixed percentage of N_2 led to an increase in the absolute amount of N_2 with rising total flow. Notably, only two conditions (0.25 mg s^{-1} He at 20 W and 0.5 mg s^{-1} He at 10 W) exhibit minimal emission, as these conditions initially operated in E-mode and later transitioned to H-mode, where the intensity was significantly higher than in previous cases. Plasma could not be sustained at 0.25 mg s^{-1} He at 10 W.

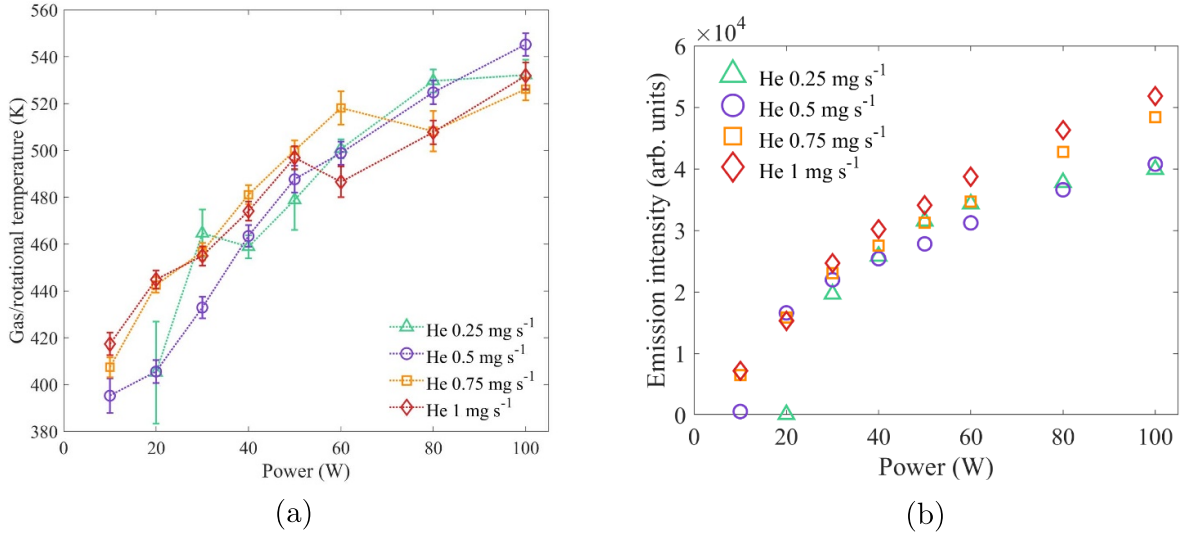

Figure 10. (a) Gas/rotational temperature and (b) emission intensity of the (0,0) SPS band head as a function of an RF power for He with 5% N_2 plasma measured in several mass flow rate of He: 0.25 mg s^{-1} (△), 0.5 mg s^{-1} (○), 0.75 mg s^{-1} (□), and 1 mg s^{-1} (◇). The error bar represents the combined values of the standard deviation of multiple measurements and systematic errors.

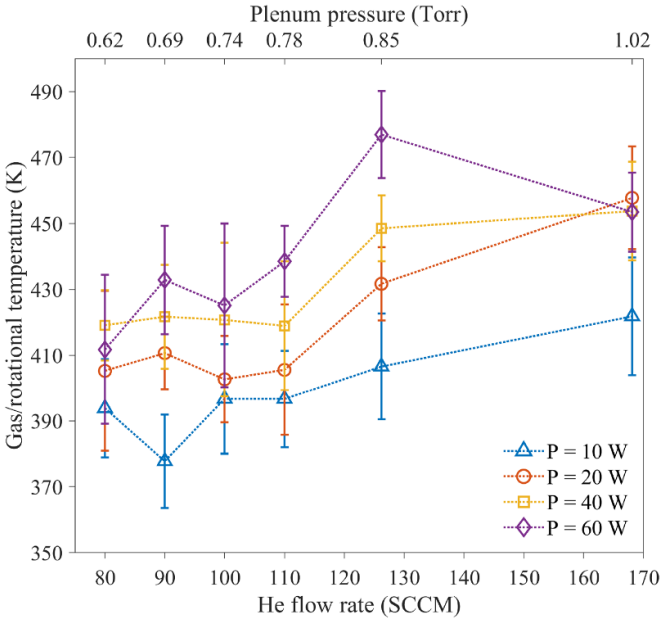

Figure 11. Gas/rotational temperature of adamantane-helium plasma as a function of He flow rate (bottom *x*-axis) or plenum pressure (top *x*-axis) plotted in several RF powers: 10 W (△), 20 W (○), 40 W (□), and 60 W (◇). The error bar represents the combined values of the standard deviation of multiple measurements and systematic errors.

The dependence of gas temperature on discharge pressure by varying the helium flow rate is presented in figure 11. Increasing He flow from 80 SCCM to 168 SCCM (corresponding to 97% and 98.5% of the total flow, respectively) while keeping the adamantane amount fixed has minimal effect on gas temperature, indicating that the primary heating source is the energy released from adamantane, as observed in the study of adamantane dependence in figure 9. The slight temperature increase is likely due to a higher collision frequency resulting from increased pressure [7]. However, the temperature rise remains modest, only 20 K at low power and up to 70 K at high power, which is within the range of measurement deviation, making this dependence insignificant.

Finally, we also briefly investigated the use of alternative Swan bands. The next strongest bands after C_2 $\Delta v = 0$ transition include $\Delta v = +1$ and -1, as shown in figure 12. The top pane shows a fair spectral fit in the $\Delta v = +1$ series, where an overlapping He emission line at 471.3 nm coincides precisely with the (2,1) transition. This overlap required subtraction, as indicated by the sinking black chain line at He I in the figure. In this rovibrational series, the intensity is two orders of magnitude weaker than of the $\Delta v = 0$ transition, resulting in a low signal-to-noise ratio, which consequently leads to unreliable the determinations of T_{rot} and T_{vib}. For $\Delta v = -1$, on the other hand, seems to fit well from the lowest $v = 0$ to $v = 4$ levels with high-resolution of rotational distribution. Higher vibrational levels are not spectrally resolved, displaying a non-Boltzmann distribution in a Boltzmann plot. The intensity here is an order of magnitude higher than that of the $\Delta v = +1$. The estimated T_{rot} and T_{vib} were 700 and 7600 K, respectively, slightly higher than those obtained in figure 6. Given the confidence in gas temperature estimates from the $\Delta v = 0$ transition, T_{rot} measured from the $\Delta v = -1$ transition may not accurately represent the gas temperature in the current study. Previous studies have shown that $\Delta v = -1$ and $+1$ C_2 transitions can reliably estimate gas temperature in high-temperature plasmas where T_{rot} is comparable to T_{vib}, as observed in high-pressure CO_2 plasma [16].

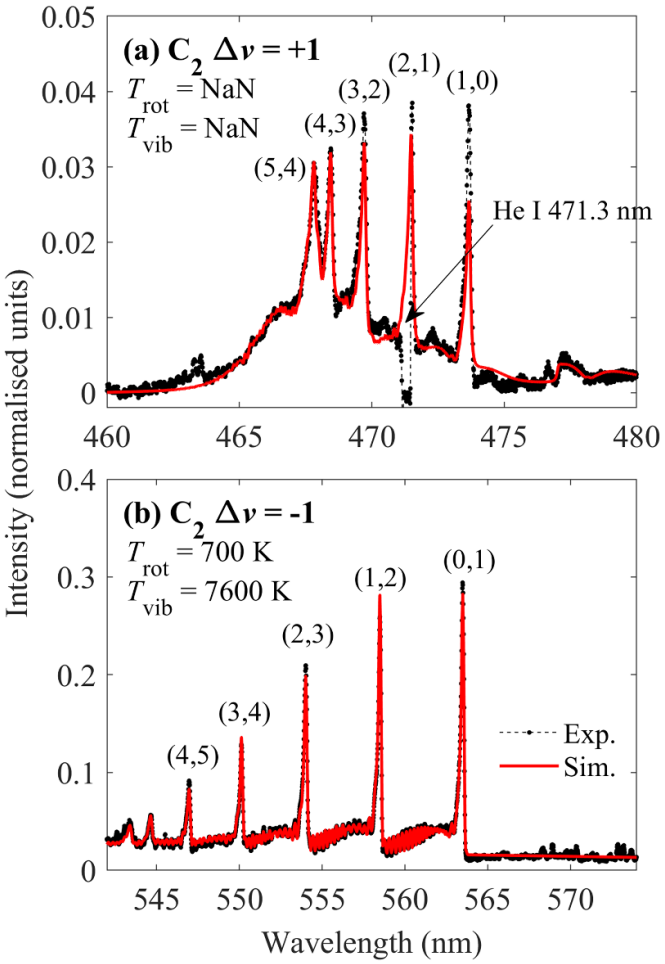

Figure 12. Examples of experimental (— · —) and simulated (——) spectral fits of C_2 Swan bands for an adamantane-helium mixture at 60 W RF power: (a) $\Delta v = +1$ series fit, where T_{rot} and T_{vib} cannot be determined due to the interference of He I 471.3 nm. (b) $\Delta v = -1$ band, showing $T_{rot} = 700$ K and $T_{vib} = 7600$ K. Vibrational transitions (X', X'') is labelled at each band head, with X denoting the vibrational state. Intensities of both fits are normalised with respect to the (0,0) Swan band.

5. Applications across various fields

The information of the neutral gas temperature can provide valuable insights in several areas of research and development. The application to electrothermal plasma thrusters using hydrocarbon propellants is increasingly important for low-budget space missions due to their storage and cost-effective advantages. Originally, the PR thruster was developed to gain more thrust by neutral gas heating via I-N CEX collisions from RF plasma [3, 4]. With confidence on the results measured from N_2, the total thrust (F_{tot}), thermal exhaust gas velocity (v_{ex}), and thrust gain (G) can be estimated by equations (15)–(17), respectively [2, 3, 53]

$$F_{tot} = F_{pl} + F_{cg} = \dot{m} v_{ex}, \tag{15}$$

$$v_{ex} = \sqrt{\frac{8 k_B T_g}{\pi M}}, \tag{16}$$

$$G = F_{pl}/F_{cg} = (F_{tot} - F_{cg})/F_{cg} \tag{17}$$

where $\dot{m}$ is the mass flow rate, F_{pl} is the thrust generated by the plasma only, F_{cg} is the axial force generated by the cold gas (without plasma), M is the molar mass in kilograms. For a 1 mg s^{-1} adamantane, the gas temperature is 480 K for 10 W and 750 K for 100 W. By using these equations, the calculated F_{tot} is 0.27 and 0.34 mN compared to a calculated F_{cg} of 0.22 mN, yielding a thrust gain of 23%–54% when assuming all thermal energy converts to kinetic energy. These values fall within the range measured in PR thrusters for a 100 SCCM Ar plasma at 20 to 50 W, as reported by Tsifakis *et al* [53], and 52.5 SCCM xenon plasma at 10 W to 70 W reported by Charles *et al* [2]. Furthermore, understanding the OES of adamantane not only helps analyse the performance of the thruster without performing thrust measurements [2], but it could support future investigations into alternative hydrocarbon propellants, such as naphthalene or camphor [22].

Adamantane has become a popular reactant for synthesising a diamond like carbon (DLC) thin film to improve the material surface properties, such as mechanical, chemical and physical durability [57, 58]. In plasma processing, parameters like concentration, pressure, and temperature are crucial, as they influence the final properties of the product. Previous studies have reported that the gas temperature has been shown to affect the hydrocarbon chemical reactions, particularly dehydrogenation [59], similar to the case where hydrocarbon conversion rates increase with increasing wall temperature [60]. Variations in species concentration due to the change in temperature impact DLC synthesis performance [58]. Therefore, evaluating a gas temperature via non-invasive method is valuable for plasma characterisation, as initially explored in section 4.5, where the use of He as a buffer gas replicates plasma process conditions [56].

From an astrophysics perspective, the emission spectra of adamantane and if fragments (e.g. C_2) as part of the diamondoid species, has been widely observed in interstellar media, especially in stars such as Elias 1 and HD 97048 [24, 25, 61]. With the knowledge of adamantane optical spectrum, it can be used to identify the presence of these species or their dissociation products in bright, distant interstellar environments. Studying the rotational and vibrational temperatures of C_2 via rovibrational bands could provide valuable information as a complement to traditional IR spectroscopy [24, 61]. If the rotational mode is in equilibrium with the translational mode, the local gas temperature in stellar regions can be determined, which is a crucial property for characterizing interstellar conditions.

6. Conclusions

The emission spectra of adamantane plasma with trace additions of N_2 and substantial additions of He were investigated to characterise gas temperatures, mainly in the context of electrothermal plasma thrusters application. OES was employed to determine the rotational temperature of excited diatomic molecules of N_2 SPS and C_2 Swan bands, using rovibrational fitting via MassiveOES software. The (0,0) transitions for both species exhibited minimal interference, identifying this

spectral range as suitable for temperature diagnostics. Initial experiments with pure N_2 plasma confirmed the accuracy of gas temperature determination, showing that gas temperature increases with rising RF power and discharge pressure. The rotational temperatures from the (0,0) N_2 and (0,0) C_2 bands were taken as equivalent to the gas temperature, assuming rapid thermalisation.

For adamantane plasma with a trace amount of N_2, the N_2 content was kept minimal to approximate conditions of pure adamantane in the plasma. The gas temperature increased with both RF power and adamantane flow rate, consistent with pure N_2 plasma results. The higher temperature found in adamantane plasma compared with pure N_2 is likely due to additional energy from the exothermic dissociations of adamantane. A power balance model analysis suggested that these measured temperatures would be accurate if the degree of dissociation was precisely identified. To enhance the visibility of C_2 spectra produced by adamantane, a large amount of He was added to increase light emission intensity. In this configuration, helium significantly influences the plasma properties, making this setup relevant to applications such as plasma processing. Similarly, the gas temperature obtained from C_2 emission increases with increasing power and adamantane flow. However, temperatures stabilised at mid-range power levels, likely due to C_2 saturation, which limits further energy absorption. An additional experiment with He-N_2 plasma confirmed that helium did not cause this steady temperature, indicating the behaviour is specific to adamantane dissociation.

The pressure dependence on the gas temperature was also examined, showing little to no effect across the entire power range. Alternatively, the C_2 $\Delta v = +1$ transition was unsuitable for temperature determination due to overlap with He emission lines, while temperature measurements from the C_2 $\Delta v = -1$ transition were overestimated under these conditions. With current results of gas temperature, thrust gain for an electrothermal plasma thruster using adamantane can be predicted. Beyond propulsion applications, the behaviour of adamantane plasma with a buffer gas is relevant to DLC thin-film synthesis, where gas temperature impacts key reaction pathways. Additionally, the resolved rovibrational spectra of C_2 offer a spectral signature that could provide information on diamondoid species in interstellar media.

Solid propellants like adamantane offer outstanding advantages over gaseous propellants due to their higher storage density, enabling lighter, non-pressurised tanks and propellant mass per unit volume. Calculation shows that solid propellants can deliver performance comparable to gaseous alternatives. Compared to resistojets, which require preheating, the Pocket-Rocket can instantly heat gas without additional processes. Although ion thrusters achieve a higher specific impulse, they demand greater system complexity and power. Adamantane-based Pocket-Rocket thrusters present an alternative and appealing solution for satellites seeking low power budgets and moderate performance.

Future work aims to validate the adamantane gas temperature through direct thrust measurement. Alternative rovibrational transitions, such as CH bands or N_2^+, may serve as additional species for gas temperature estimation. A more comprehensive study could incorporate electrical diagnostics and mass spectrometry, especially at mid-range power levels where coupling transitions occur. The spectroscopic analysis may also be extended to other solid hydrocarbons, such as naphthalene or camphor, to explore their suitability as alternatives to adamantane.

Data availability statement

All data that support the findings of this study are included within the article (and any supplementary files). The raw data obtained from this paper may be available upon reasonable request.

Acknowledgment

This research was funded by the SP3 laboratory. This work is a part of TL's thesis, a PhD candidate; and has been supervised by CC and RB. Special thanks to MD and DT for technical assistance. Fruitful discussions and suggestions with Dr Joshua Machacek and Assoc Prof Dr Apisit Songsasen are also acknowledged.

Conflicts of interest

The authors declare that they have no known competing financial interests or personal relationships that could have appeared to influence the work reported in this paper.

ORCID iDs

Thimthana Lee https://orcid.org/0009-0005-6862-4607
Mahdi Davoodianidalik https://orcid.org/0000-0002-5430-8540

References

[1] Goebel D M, Katz I and Mikellides I G 2023 *Fundamentals of Electric Propulsion* (Wiley)
[2] Charles C, Boswell R W, Bish A, Khayms V and Scholz E F 2016 *Front. Phys.* **4** 19
[3] Charles C and Boswell R 2012 *Plasma Sources Sci. Technol.* **21** 022002
[4] Greig A, Charles C, Hawkins R and Boswell R 2013 *Appl. Phys. Lett.* **103** 074101
[5] Bruggeman P J, Sadeghi N, Schram D and Linss V 2014 *Plasma Sources Sci. Technol.* **23** 023001
[6] Davis G P and Gottscho R A 1983 *J. Appl. Phys.* **54** 3080–6
[7] Zhang Q, Shi D, Xu W, Miao C, Ma C, Ren C, Zhang C and Yi Z 2015 *AIP Adv.* **5** 057158
[8] Laux C O and Kruger C H 1992 *J. Quantum Spectrosc. Radiat. Transfer* **48** 9–24
[9] Donnelly V and Malyshev M 2000 *Appl. Phys. Lett.* **77** 2467–9
[10] Phillips D 1976 *J. Phys. D: Appl. Phys.* **9** 507
[11] Bai B, Sawin H H and Cruden B A 2006 *J. Appl. Phys.* **99** 013308
[12] Karakas E, Donnelly V M and Economou D J 2013 *J. Appl. Phys.* **113** 98

[13] Pearse R W B, Gaydon A G, Pearse R W B and Gaydon A G 1976 *The Identification of Molecular Spectra* vol 297 (Chapman and Hall London)
[14] Lombardi G, Bénédic F, Mohasseb F, Hassouni K and Gicquel A 2004 *Plasma Sources Sci. Technol.* **13** 375
[15] Cruden B A, Rao M, Sharma S P and Meyyappan A M 2002 *J. Appl. Phys.* **91** 8955–64
[16] Carbone E, D'Isa F, Hecimovic A and Fantz U 2020 *Plasma Sources Sci. Technol.* **29** 055003
[17] Brockhinke A, Letzgus M, Rinne S and Kohse-Höinghaus K 2006 *J. Phys. Chem.* A **110** 3028–35
[18] Pellerin S, Musiol K, Motret O, Pokrzywka B and Chapelle J 1996 *J. Phys. D: Appl. Phys.* **29** 2850
[19] Wang Q, Doll F, Donnelly V M, Economou D J, Sadeghi N and Franz G F 2007 *J. Phys. D: Appl. Phys.* **40** 4202
[20] Britun N, Gaillard M, Ricard A, Kim Y, Kim K and Han J 2007 *J. Phys. D: Appl. Phys.* **40** 1022
[21] Bol'shakov A A, Cruden B A and Sharma S P 2004 *Plasma Sources Sci. Technol.* **13** 691
[22] Lee T, Davoodianidalik M, Tsifakis D, Boswell R W and Charles C 2025 *Acta Astronaut.* **226** 427–38
[23] Dietz P, Gärtner W, Koch Q, Köhler P E, Teng Y, Schreiner P R, Holste K and Klar P J 2019 *Plasma Sources Sci. Technol.* **28** 084001
[24] Pirali O, Boudon V, Oomens J and Vervloet M 2012 *J. Chem. Phys.* **136** 53
[25] Candian A, Bouwman J, Hemberger P, Bodi A and Tielens A G 2018 *Phys. Chem. Chem. Phys.* **20** 5399–406
[26] Stauss S, Ishii C, Pai D Z, Urabe K and Terashima K 2014 *Plasma Sources Sci. Technol.* **23** 035016
[27] Bouwman J, Horst S and Oomens J 2018 *ChemPhysChem* **19** 3211–8
[28] Voráč J, Synek P, Potočňáková L, Hnilica J and Kudrle V 2017 *Plasma Sources Sci. Technol.* **26** 025010
[29] Voráč J, Synek P, Procházka V and Hoder T 2017 *J. Phys. D: Appl. Phys.* **50** 294002
[30] Voráč J, Kusýn L and Synek P 2019 *Rev. Sci. Instrum.* **90** 123102
[31] Kramida A, Yu R and Reader J (NIST ASD Team) 2023 NIST Atomic Spectra Database (ver. 5.11) (available at: https://physics.nist.gov/asd)
[32] Herzberg G 1950 *Molecular Spectra and Molecular Structure* vol 1 (van Nostrand)
[33] Huber K 2013 *Molecular Spectra and Molecular Structure: IV. Constants of Diatomic Molecules* (Springer Science & Business Media)
[34] Lofthus A and Krupenie P H 1977 *J. Phys. Chem. Ref. Data* **6** 113–307
[35] Prasad C and Bernath P 1994 *Astrophys. J.* **426** 812–21
[36] Brooke J S, Bernath P F, Schmidt T W and Bacskay G B 2013 *J. Quantum Spectrosc. Radiat. Transfer* **124** 11–20
[37] Dunham J 1932 *Phys. Rev.* **41** 721
[38] Bernath P F 2020 *Spectra of Atoms and Molecules* (Oxford University Press)
[39] Western C M 2017 *J. Quantum Spectrosc. Radiat. Transfer* **186** 221–42
[40] Le Roy R J 2017 *J. Quantum Spectrosc. Radiat. Transfer* **186** 167–78
[41] Wang Q, Koleva I, Donnelly V M and Economou D J 2005 *J. Phys. D: Appl. Phys.* **38** 1690
[42] Faure G and Shkol'Nik S 1998 *J. Phys. D: Appl. Phys.* **31** 1212
[43] Ho T S, Charles C and Boswell R W 2017 *Front. Phys.* **4** 55
[44] Johnson A W and Fowler R 1970 *J. Chem. Phys.* **53** 65–72
[45] De Benedictis S and Dilecce G 1995 *Chem. Phys.* **192** 149–62
[46] Schabel M, Donnelly V, Kornblit A and Tai W 2002 *J. Vac. Sci. Technol.* A **20** 555–63
[47] Hoskinson A R, Hopwood J, Bostrom N W, Crank J A and Harrison C 2011 *J. Anal. Atom. Spec.* **26** 1258–64
[48] Oshima M 1981 *Japan J. Appl. Phys.* **20** 683
[49] Xuechu L and Nanquan L 1980 *Chem. Phys. Lett.* **75** 110–4
[50] Setser D, Stedman D and Coxon J 1970 *J. Chem. Phys.* **53** 1004–20
[51] Erman P 1980 *Phys. Scr.* **22** 108
[52] Duten X, Rousseau A, Gicquel A and Leprince P 1999 *J. Appl. Phys.* **86** 5299–301
[53] Tsifakis D, Charles C and Boswell R 2020 *Front. Phys.* **8** 34
[54] Lieberman M and Lichtenberg A 2005 *Principles of Plasma Discharges and Materials Processing* 2nd edn (Wiley-Interscience)
[55] Greig A, Charles C and Boswell R W 2015 *Front. Phys.* **3** 84
[56] Sun Z, Lin C, Lee Y, Shi J, Tay B and Shi X 2000 *J. Appl. Phys.* **87** 8122–31
[57] Umeno M, Noda M, Uchida H and Takeuchi H 2008 *Diam. Relat. Mater.* **17** 684–7
[58] Zeze D, O'toole E, Crawford R, Cui N, Anderson C and Brown N 1998 *Surf. Interface Anal.* **26** 896–902
[59] Ashfold M N, May P W, Petherbridge J R, Rosser K N, Smith J A, Mankelevich Y A and Suetin N V 2001 *Phys. Chem. Chem. Phys.* **3** 3471–85
[60] García-Moncada N, Cents T, van Rooij G and Lefferts L 2021 *J. Energy Chem.* **58** 271–9
[61] Steglich M, Huisken F, Dahl J, Carlson R and Henning T 2011 *Astrophys. J.* **729** 91